Magnetization dynamics and cone angle precession in permalloy rectangles

Nils Kuhlmann,[*] Andreas Vogel, and Guido Meier

*Institut für Angewandte Physik und Zentrum für Mikrostrukturforschung, Universität Hamburg, Jungiusstrasse 11,
DE-20355 Hamburg, Germany*

Magnetization dynamics in pairs of submicrometer-sized permalloy rectangles are studied by means of broadband-ferromagnetic resonance measurements. The coupling strength of neighboring elements depends on their center-to-center distance. The stray field of one rectangle decreases the local effective field at the position of the other rectangle. Pairs consisting of two different rectangles, like in a conventional all-metal lateral spin-valve device, are studied. Moreover, the cone angles of the precessional motion of the magnetization at ferromagnetic resonance are determined using transport measurements. Large cone angles of up to $13.7°$ are realized in a sample geometry that permits electrical insulation together with a small distance between the permalloy rectangles and the exciting coplanar waveguide.

PACS number(s): 75.75.−c, 76.50.+g, 85.75.−d

I. INTRODUCTION

Magnetization dynamics of submicrometer-sized ferromagnets have been in the focus of interest experimentally[1–3] and theoretically[4–6] for a number of years. Potential applications in ultrafast nonvolatile magnetic storage cells and logical units fuel this attention. Reliable and applicable magnetization configurations in nanostructures require an accurate knowledge of the underlying spin-wave eigenmodes and eigenfrequencies since switching times are more and more pushed into the regime of precessional periods. The spectrum of confined spin waves in magnetic elements reflects the static magnetization and the concomitant internal fields. The quantization of spin waves due to the spatial confinement was observed[7,8] and it is now understood that the inhomogeneous internal field in nonellipsoidal elements leads to localization of spin-wave modes.[4,9] Substantial effort has also been made in the understanding of inhomogeneously magnetized stripes[10,11] and in even more complicated structures like ferromagnetic disks with a vortex,[1,12–14] rings with different spin-wave eigenmodes in varying magnetic field directions,[15] or squares.[2,3,16]

We study the ferromagnetic resonance in rectangular nanostructures. Dipolar coupled lateral ferromagnetic permalloy elements are arranged in pairs, see Fig. 1(a). Such structures play an important role in all-metal lateral spin-valve devices[17–20] that consist of two bar-shaped electrodes separated by a small gap. In the low-frequency regime, all-metal lateral spin-valve devices are workhorses in spintronics as they provide reliable injection, manipulation, and detection of spin-polarized currents.[17–20] Recently, the basic concepts of spintronic devices have been extended by dynamical effects, e.g., spin rectification in the spin dynamo[21] or spin pumping[22] in the spin battery.[23] The spin-pumping effect generates a pure spin current at the interface between a ferromagnet with a precessing magnetization and a normal metal and is useful for spin injection. The development of a highly efficient spin source by spin injection of a precessing magnetization can provide a solution to the vision of spintronic devices.

In the first part of this work, the fundamental ferromagnetic resonance mode in permalloy ($Ni_{80}Fe_{20}$) rectangles and its dispersion relation is characterized by broadband ferromagnetic-resonance (FMR) spectroscopy using a vector-network analyzer. In view of their applicability in transport spintronics, the permalloy rectangles are called electrodes from here on. The stray-field interaction between the electrodes is studied by varying their center-to-center distance. In the second part, transport measurements at room temperature in combination with high-frequency excitation are used to detect the precessional motion of the magnetization in a single electrode at resonance. The sample design with an insulating layer provides shorter distances between the stimulating coplanar waveguide and the excited electrodes compared to other approaches.[24] Anisotropic magnetoresistance (AMR) measurements with low current densities through a single electrode probe the magnetization without perturbing the local magnetic moments. The cone angle of the precession is quantified and a high maximum value of nearly fourteen degrees is achieved. Since the efficiency of the spin-current injection in a spin battery directly depends on the cone angle,[25] these results have strong implications for spin-pumping experiments.

II. METHODS

The magnetization dynamics of ferromagnetic materials can be described by the Landau-Lifshitz-Gilbert equation[26] (LLG)

$$\frac{d\vec{m}}{dt} = -\gamma\mu_0(\vec{m} \times \vec{H}_{\mathrm{eff}}) + \frac{\alpha}{m}\left(\vec{m} \times \frac{d\vec{m}}{dt}\right), \qquad (1)$$

where $\vec{m}$ is the magnetic moment, $\vec{H}_{\mathrm{eff}}$ the effective magnetic field, γ the gyromagnetic ratio, and α the Gilbert damping parameter. The effective field $\vec{H}_{\mathrm{eff}}$ typically includes exchange, external, and demagnetization field contributions. However, the permalloy electrodes investigated exhibit a single domain structure with only small deviations of the uniform magnetization at the short edges. Hence, the exchange contribution is constant in good approximation and the macrospin model is applicable. In this model, a uniform magnetic moment density, the magnetization $\vec{M}$, is introduced. Together with the volume V, the equation $\vec{m} = V\vec{M}$ can be inserted in Eq. (1) showing that the LLG equation can also describe the magnetization dynamics of single-domain ferromagnetic nanostructures. When changing the static external magnetic
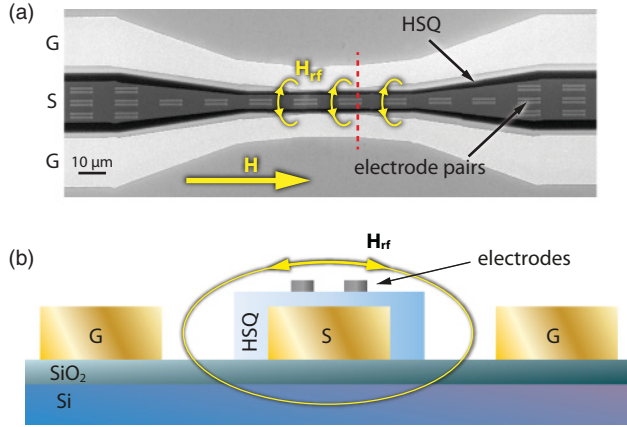
FIG. 1. (Color online) (a) Scanning-electron micrograph of permalloy electrode pairs on top of a coplanar waveguide and an insulating hydrogen silsesquioxane (HSQ) layer. (b) Sketch of the cross section of the samples for FMR measurements at the position indicated by the dashed line in (a).

field $\vec{H}$, the magnetization starts to precess. This is described by the first term on the right-hand side of Eq. (1). Due to damping, the magnetization relaxes along the direction of the external field, which is described by the second term on the right-hand side. In FMR experiments, the precession of the magnetization is maintained by continuous excitation. An rf field $\vec{H}_{rf}$ excites the electrodes near their eigenfrequency f. The energy loss due to damping is then compensated by energy transfer from the field $\vec{H}_{rf}$. For resonant excitation of the electrodes, a coplanar waveguide (CPW) is used. The first port of a vector-network analyzer sends a sinusoidal rf current through the CPW, creating the rf field $\vec{H}_{rf}$ around the central conductor. When the frequency matches the eigenfrequency of the electrodes, energy is transferred into the precession of the magnetization, which contributes to a reduction of the transmission[27] T measured at the second port of the vector-network analyzer.

Samples are prepared by electron-beam lithography and lift-off processing. The following description is in the order of fabrication. For comparison see also Fig. 1(b). The CPW consists of a 120 nm-thick Au layer evaporated on top of a SiO$_2$/Si substrate and an 8 nm-thin adhesive Cr layer. Afterwards, a layer of hydrogen silsesquioxan (HSQ) is spin coated and structured via electron-beam lithography. The layer has a thickness of approximately 200 nm and provides electric insulation of the electrodes from the CPW. The insulation is required for the transport measurements, probing the AMR of a single electrode. Subsequently, on top of the HSQ layer, the electrodes are fabricated by thermally evaporating permalloy at a base pressure of about 5×10^{-8} mbar. For the contacts of the innermost electrode, see Figs. 6(a)–6(c), the permalloy interface is cleaned via rf argon-plasma etching. Without breaking the vacuum, 2 nm Al and 50 nm Au are subsequently deposited via dc-magnetron sputtering.

The frequency of resonant excitation of ferromagnetic micro- and nanostructures can be described by the Kittel formula.[28] The geometry of the rectangular-shaped electrodes is taken into account by the corresponding demagnetization
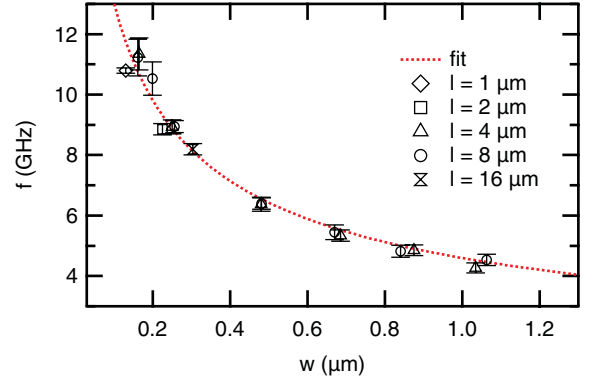

FIG. 2. (Color online) Dependence of the resonance frequency f of the electrodes on their width w. The dashed line is a fit to the experimental data following the Kittel formula, Eq. (2). The thickness of all electrodes is 30 nm. Their lengths l vary between 1 and 16 μm.

factors, and the Kittel formula reads[29]

$$f = \frac{\gamma \mu_0}{2\pi} \sqrt{\left[H + \frac{2t}{\pi w} M_s \right] \left[H + \left(1 - \frac{2t}{\pi w} \right) M_s \right]}, \quad (2)$$

where H is the absolute value of the external magnetic field in A m^{-1}, M_s the saturation magnetization in A m^{-1}, t the thickness, and w the width of the electrodes. Thus the resonance frequency can be tailored via the geometry of the electrodes, compare Fig. 2. The data in Fig. 2 are obtained for electrodes with various lengths l between 1 and 16 μm. Note that the length of the electrodes does not enter in the Kittel formula meaning that the macrospin model is a rather good approximation for the description of the resonance frequency of the electrodes.

III. EXPERIMENTAL RESULTS AND DISCUSSION

A. Magnetization dynamics of electrode pairs

Magnetization dynamics of the electrode pairs are investigated by means of a broadband ferromagnetic-resonance setup using a vector-network analyzer. The resonance frequency depends on the static external magnetic field $\vec{H}$, compare Eq. (2), which is aligned parallel to the long axes of the electrodes, see Fig. 1(a). For the broadband FMR measurements, the power of the rf excitation is 1 mW leading to a field amplitude of $H_{rf} \approx 0.07$ mT in the wider part of the CPW where most of the electrodes are located. In Fig. 3(a), a typical broadband FMR measurement is shown. In this measurement, the electrodes have the dimensions 8 μm × 800 nm × 30 nm and are denoted in the following as *short* electrodes [electrodes with dimensions 16 μm × 250 nm × 30 nm will be denoted as *long* electrodes, see Fig. 3(c)]. The electrodes are arranged in pairs like the ones shown in Fig. 1(a). The static field $\vec{H}$ is varied from −90 to +90 mT. In Figs. 3(a) and 3(c), dark color corresponds to reduced transmission. For each field step the frequency is swept and the transmission is measured. Starting with a field of $\mu_0 H = -90$ mT, the magnetizations of the electrodes are aligned parallel to the external field $\vec{H}$. With smaller field amplitudes H, the resonance frequency f decreases as predicted by the Kittel formula. For small
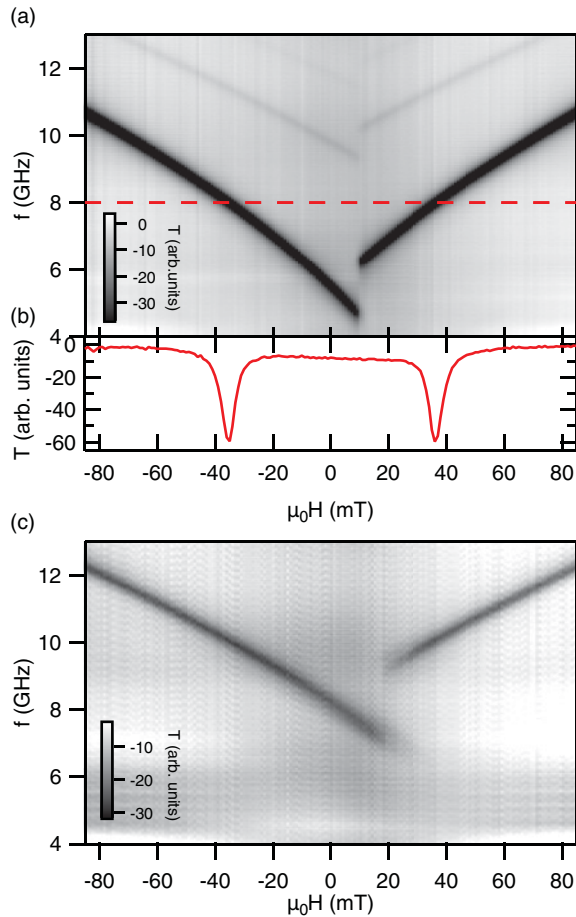
FIG. 3. (Color online) (a) Broadband FMR measurement of short electrode pairs with a center-to-center distance of 1595 nm. Dark corresponds to a reduced transmission T. (b) Transmission spectrum for a constant frequency of 8 GHz indicated in (a) by the dashed line. (c) Broadband FMR measurement of long electrode pairs with a center-to-center distance of 397 nm.

FIG. 4. (Color online) (a) Resonances of pairs of short electrodes for two different center-to-center distances d. (b) Resonance fields vs. center-to-center distance d for the short electrodes at the constant excitation frequency of $f = 8$ GHz. (c) Resonance fields in dependence on d for the long electrodes at the frequency $f = 11$ GHz.

fields in the opposite direction, the magnetizations of the electrodes remain in the former direction because of their shape anisotropy. The external field $\mu_0 H = 9$ mT (20 mT) is strong enough to switch the magnetization of the short (long) electrodes again parallel to the field direction, clearly visible in a jump of the resonance frequency.

A transmission spectrum for a constant frequency of 8 GHz is shown in Fig. 3(b). The transmission versus the static field has two minima that are symmetric around zero field. By fitting a Lorentzian to the experimental data, the resonance fields H_{res} for a given frequency are determined.

The center-to-center distance d between neighboring short electrodes has been varied between 961 and 1595 nm. It is worth noting that the edge-to-edge distance is by the half widths of both electrodes smaller than the center-to-center distance d. For each distance, measurements as shown in Fig. 3(a) are performed. The transmission minima for each frequency sweep are determined via fitting a Lorentzian to the experimental data. Resonance data are shown in Fig. 4(a) for electrode pairs with distances $d = 961$ and 1595 nm. The resonance for the electrode pairs with the shorter distance is shifted down to lower frequencies, or in other words, for
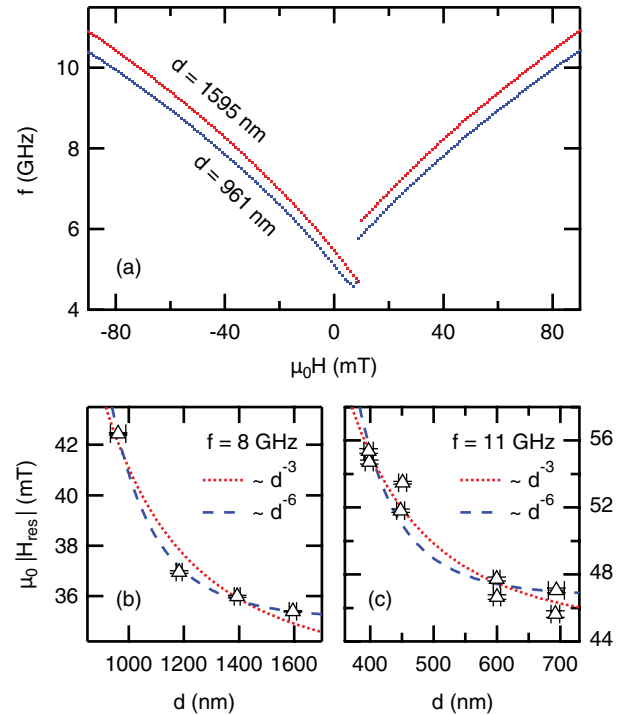
a constant frequency higher external static fields H_{res} are required to achieve FMR. For a constant frequency of 8 GHz, resonance fields for different center-to-center distances d are displayed in Fig. 4(b). For decreasing distances, the external fields required for FMR increase.

When starting the measurement at -90 mT, the magnetizations of the electrodes are oriented parallel to the external bias field. Since the electrodes are arranged in pairs, the stray field of the neighboring electrode has an impact on the local effective magnetic field at the position of the other electrode. As the stray field points antiparallel to the applied field, the local effective field is decreased. The closer the electrodes of one pair get to each other, the stronger the stray field is. Since the effective field needed for resonant excitation stays the same, higher external fields have to compensate the stray fields. Figure 4(b) shows resonance fields for pairs of short electrodes, whereas Fig. 4(c) shows results for pairs of long electrodes. For the long electrodes, the center-to-center distance is varied from 397 nm to 694 nm. Since the resonance frequency depends on the width w of the electrodes, the absolute value of H_{res} is different for short and long electrodes. Theoretical curves to the measured data are suggested as guides to the eye. The physical motivation for the d^{-3} and d^{-6} dependence on H_{res} is a dipolar and an induced dipolar interaction,[13] respectively. The number of measured distances d is relatively small, so the true character of the interaction remains arguable. In the case of the short electrodes, the d^{-6} law seems to fit better, whereas for the long electrodes d^{-3} is preferable. This can be attributed to the different shape anisotropies
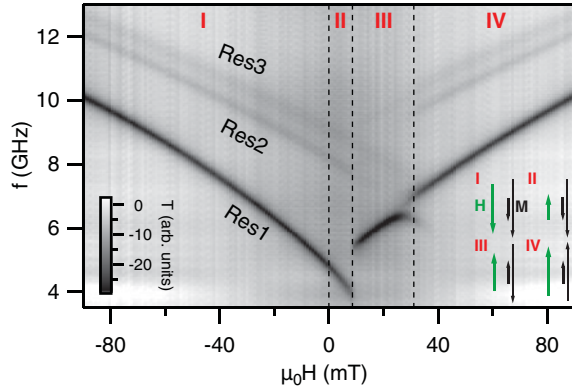
FIG. 5. (Color online) Broadband FMR measurement of electrode pairs in spin-valve geometry. Dark corresponds to reduced transmission T. Four magnetic field regions I–IV can be distinguished. They depend on the magnetic configuration of the electrodes as sketched in the inset.

corresponding to the different electrode geometries. The shape anisotropy is stronger for the long electrodes, meaning that a stray field induced magnetization change is suppressed, leaving the d^{-3} law, see Fig. 4(c). In comparison, the short electrodes have a smaller shape anisotropy, allowing induced magnetization changes and creating the d^{-6} dependence, observed in Fig. 4(b).

Up to this point, pairs of geometrically equal electrodes have been investigated. For spin-transport experiments, electrode pairs with different geometries are required.[17–20] In the following, pairs consisting of a short and a long electrode, that we address as spin-valve geometry, are studied. Two different resonances are expected for this type of electrode pairs. For the measurement shown in Fig. 5, electrode pairs with spin-valve geometry are deposited on top of the CPW with a center-to-center distance of $d = 658$ nm, corresponding to an edge-to-edge distance of 113 nm.

Three resonances addressed as Res1, Res2, and Res3 are observed for electrodes in spin-valve geometry. The above characterization of each electrode type allows the following interpretation of this measurement. Res1 corresponds to the resonance of the short electrodes. Both, frequency range and switching fields, are in accordance with the measurements performed at short electrodes, compare Fig. 3(a). Res2 corresponds to the resonance of the long electrodes, see Fig. 3(c). Res3 is a higher-order spin-wave mode of the short electrodes, also visible in the center region of the measurement shown in Fig. 3(a).

Four regions I–IV are introduced in Fig. 5, each for a certain magnetic configuration of the electrodes with respect to the direction of the external magnetic field $\vec{H}$. A schematic of the magnetization directions of the short and long electrode along with the external field is shown in the inset of Fig. 5. In the measurements, the external magnetic field is swept from -90 to $+90$ mT. In region I, the external field and the magnetizations of short and long electrodes are aligned parallel to each other. In region II, the external field changes its direction while the magnetizations of short and long electrodes both remain in their former direction due to their shape anisotropy. At a field of $\mu_0 H = 8$ mT, the external field

is strong enough to switch the magnetizations of the short electrodes visible in the jump of Res1 in Fig. 5, compare Fig. 3(a). In region III, external field and short electrodes are aligned parallel, whereas the long electrodes are aligned antiparallel to both. The intensity of the signal of the resonance of the long electrodes (Res2) decreases, but the resonance corresponding to the short electrodes (Res1) is getting stronger compared to region I. In general, higher absorption, i.e., a stronger resonance is caused by more material at FMR. This means that in region III more material is resonantly excited at the resonance frequency of the short electrodes than in region I. Given that in region I all the short electrodes should already be at resonance, a possible interpretation is that the long electrodes dynamically couple[30,31] to the stray field of the magnetization of the short electrodes. Thus, in region III, the long electrodes may precess with the resonance frequency of the short electrodes, giving rise to the higher absorption. Note that near the change from region III to IV an anticrossing in Res1 is visible. The resonance is bent down to lower frequencies. The origin of this feature is not the subject of this work but it would be interesting to take a closer look at it in a future study. Finally, in region IV, the external field is strong enough to switch the magnetization of the long electrodes to parallel configuration of external field and magnetizations of short and long electrodes. Compared to the resonance of geometrically equal pairs of long electrodes, see Fig. 3(c), the switching field has changed from approximately 20 to 32 mT. In region III, the short electrodes are aligned antiparallel to the long electrodes, thus the stray field of the short electrodes enforces the magnetization of the long electrodes against the external field. This causes a retardation of the switching of the long electrodes to higher external bias fields.

B. Cone angle magnetization precession

The precession of the magnetization at ferromagnetic resonance can be characterized by the cone angle θ. Since the injected spin current mainly depends on the cone angle,[25] it is of great importance for spin-pumping experiments. In the following, the angle θ in single, short and long electrodes is determined by means of transport experiments.

A lock-in amplifier is connected to a single electrode via Au leads, see Figs. 6(a)–6(c). The contacted electrode is located in a narrowed area of the CPW. In this region, the amplitude of the rf field $\vec{H}_{rf}$ is increased. A current is sent through the electrode and the resistance is measured. The current density is at maximum 2.7×10^8 A m^{-2} and thus cannot induce dynamics by spin torque in permalloy.[32] Due to the precessing magnetization at FMR, magnetization components transverse to the applied current arise. This results in a decrease of the resistance because of the AMR, which depends on the angle between the magnetization and the local current density.[33] Here, this angle is the cone angle θ, see Fig. 6(d), and the resistance of the electrode reads

$$R(\theta) = R_\parallel - \Delta R \sin^2 \theta \qquad (3)$$

with $\Delta R = R_\parallel - R_\perp$, where $R_\parallel$ is the resistance of parallel and $R_\perp$ of perpendicular alignment of magnetization and current density. The resistance decreases with $\Delta R \sin^2 \theta$ when the magnetization precesses with the cone angle θ. With Eq. (3)
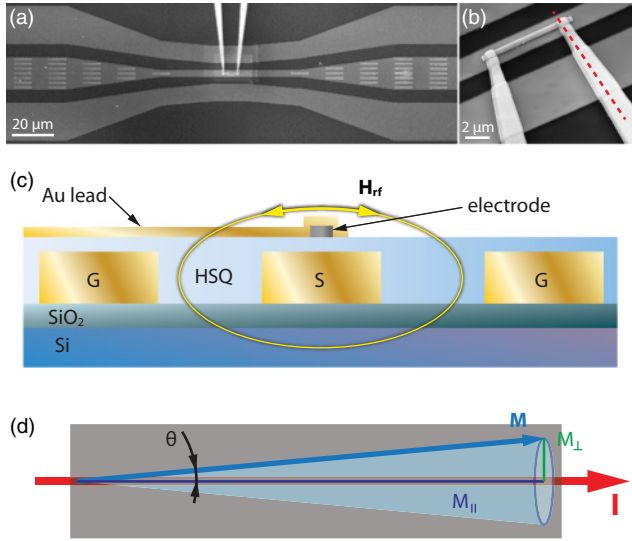
FIG. 6. (Color online) (a) Scanning-electron micrograph of short electrodes on top of a CPW. A single electrode is contacted with Au leads for AMR detection. (b) Scanning-electron micrograph of the contacted electrode, compare center part of (a). (c) Sketch of the cross section of the samples for cone angle measurements at the position indicated by the dashed line in (b). (d) Sketch of an electrode (grey) at resonance. A current I is sent through the electrode while its magnetization precesses with the cone angle θ.

and a measured resistance drop at resonance of ΔR_res, the cone angle

$$\theta = \arcsin \sqrt{\frac{\Delta R_\mathrm{res}}{\Delta R}} \qquad (4)$$

can be calculated when assuming a uniform precession mode.

For the calculation of the cone angle, the resistance change $\Delta R = R_\parallel - R_\perp$ between the magnetization oriented parallel and perpendicular to the current has to be measured. This is done by applying a static external field parallel and transverse to the long axes of the electrodes, driving the magnetization into saturation in the corresponding directions. The resistances $R_\parallel$ and $R_\perp$ are determined in these saturated states.

To determine the cone angle, the magnetic field is swept while the resistance R of the electrode and the transmission T through the waveguide is measured. This is done for two different excitation frequencies. In the data processing, the two values of R and T for the same field but different frequencies are subtracted to separate out the resistance signal from temperature-dependent drifts and cable resistances. This results in a transmission difference $\Delta T = T_{f_2} - T_{f_1}$ and a resistance difference $\Delta R_\mathrm{FMR} = R_{f_2} - R_{f_1}$ shown in Fig. 7. To understand the shape of the signals in Fig. 7, another look at Fig. 3(b) is helpful. For transmission spectra at different frequencies, the transmission minima are at different external fields. When a transmission spectrum of a low frequency f_1 is subtracted from a spectrum at a higher frequency f_2, the transmission minima corresponding to f_1 are folded up in the difference signal $\Delta T = T_{f_2} - T_{f_1}$, compare Fig. 7(a). The data shown in Fig. 7(b) were recorded at different frequencies f_1 and f_2 and demonstrate the dependence of the location of the minima on these frequencies.
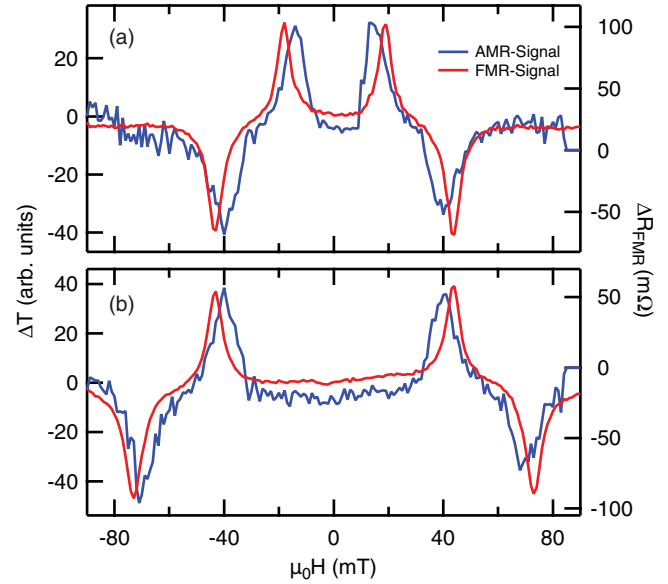

FIG. 7. (Color online) (a) Transmission difference $\Delta T = T_{f_2} - T_{f_1}$ of an ensemble of electrodes and resistance difference $\Delta R_\mathrm{FMR} = R_{f_2} - R_{f_1}$ of a single electrode vs. the external magnetic field. The constant excitation frequencies were $f_1 = 6.5$ GHz and $f_2 = 8.0$ GHz. (b) ΔT and ΔR_FMR at $f_1 = 8.0$ GHz and $f_2 = 9.5$ GHz.

The resemblance of the resistance signal to the ferromagnetic resonances in Fig. 7 is striking. The transmission decreases when the ensemble of electrodes is at resonance. The magnetizations of the electrodes precess and give rise to transverse components of the magnetization. The resistance of the single electrode decreases at resonance due to the AMR.

The resistance signals ΔR in Fig. 7 are slightly shifted to smaller fields in comparison to the FMR signal ΔT. The FMR signal is an ensemble measurement and all electrodes on the waveguide contribute to the measured transmission. Most of the electrodes are located in the wide, outer parts of the signal line and are neighbored by other electrodes, see Fig. 6(a). They are separated from each other by 1.8 μm [direction of columns in Fig. 6(a)]. Although the separation minimizes the influence, the stray fields of the surrounding electrodes superimpose and reduce the local effective field. In contrast, the resistance signal ΔR displays the resonance of a single electrode in the innermost part of the narrowed signal line. This electrode is well separated from other electrodes and can safely be considered as isolated from other stray fields. The different stray-field strengths give rise to the small difference of resonance fields for isolated and ensemble measurements in Fig. 7.

The cone angles θ are calculated according to Eq. (4). Note that in the present model, the precessional motion is described by a cone with a circular base area. Since the width of the electrodes is much larger than their thickness, the motion will be a cone with an elliptical base area in reality. The deduced cone angles are therefore averaged values.

We found that the cone angles θ depend on the width w of the electrodes. Short and long electrodes are measured. For the short electrodes, we obtain cone angles of up to $(13.7 \pm 0.7)^\circ$. The largest measured value for the long electrodes is

TABLE I. Overview of measured cone angles θ. Specified are the widths of electrodes w, the widths of the signal line of the CPW w_{CPW}, and the external magnetic fields H_{res} where the electrodes are at resonance.

electrode type/w (nm)	w_{CPW} (μm)	$\mu_0 H_{res}$ (mT)	θ (°)
short/800	3	14	13.7 ± 0.7
short/800	5	16	9.4 ± 0.7
long/250	3	40	9.0 ± 0.7
long/250	5	41	4.5 ± 0.6

$\theta = (9.0 \pm 0.7)°$. As already mentioned, the demagnetization field defined by the shape of the electrodes is stronger for the long than for the short electrodes. The demagnetization field pulls the magnetizations in the direction of the long axes of the electrodes and the cone angle is reduced. Consequently, largest cone angles are found in the short electrodes.

Furthermore, the width of the central area of the signal line of the CPW has been varied. The narrower the signal line is, the higher is the current density, and hence the amplitude of the rf field $\vec{H}_{rf}$ that excites the precessional motion. For cone angle measurements, an rf excitation power of 5 mW is used. Narrowing the signal line from 5 to 3 μm leads to an increase of the rf field amplitude from approximately 0.5 to 0.7 mT and thus considerably enhances the cone angle θ. For the short electrodes, the cone angle increases from $(9.4 \pm 0.7)°$ to $(13.7 \pm 0.7)°$. The results are summarized in Table I. In addition to the width of the signal line and the electrodes, the resonance fields H_{res} are indicated. This is done because the cone angle also depends on the external field $\vec{H}$. Due to the Zeeman-energy contribution, the magnetizations are pulled in the direction of the long axes of the electrodes. With higher external fields, the force that pulls the magnetizations back into the equilibrium direction increases, thus the cone angle θ decreases. In the measurement shown in Fig. 7(a), the resonances at ± 40 mT correspond to a cone angle of $(12.3 \pm 0.6)°$. In contrast, the resonances at ± 14 mT yield $\theta = (13.7 \pm 0.7)°$.

To clarify whether the measured signals are caused or not caused by bulk rectification,[21,25,34] the sample was tilted in the external field, so that field and equilibrium magnetizations are not aligned parallel. The analysis in Ref. 25 shows that in a comparable geometry, dc currents are induced for tilting angles of 5° and larger. Measurements that we performed with a misalignment of 5° showed no difference but random noise compared to measurements with correct alignment. Hence, it can be ruled out that the measured signals are caused by the bulk rectification effect but are caused by the precessional motion of the magnetization of the electrodes and the resulting anisotropic magnetoresistance.

IV. CONCLUSION

Research on metal-based spintronic devices benefits from microwave techniques. Continuous-wave excitations of such devices can provide insight into the intrinsic dynamics of charge and spin transport and give access to important parameters like spin-relaxation times and lengths.

We comprehensively characterized the magnetization dynamics of permalloy electrodes for spintronic devices. A broadband ferromagnetic-resonance setup was used to investigate the dipolar coupling of electrode pairs. In the sample design with pairs of geometrically equal electrodes, a decreasing center-to-center distance results in higher resonance fields. The measurements on pairs in spin-valve geometry demonstrate that a separate excitation of each electrode type is possible. Even when the electrodes of one pair are in close proximity, over a wide field range, the resonance frequencies are well separated. Consequently, the present sample geometry is adequate for device applications, e.g., for spin pumping.

Spin pumping[22] in the spin battery[23] proposed by Brataas *et al.* drives a pure spin current from a ferromagnetic element into an adjacent normal metal. A device to create and detect the pumped spin current is similar to conventional all-metal lateral spin valves.[17–19] Two bar-shaped ferromagnetic electrodes with differing shapes are interconnected with a normal-metal strip. The systematic characterization of the magnetization dynamics of pairs of short and long electrodes as well as of pairs in spin-valve geometry are therefore highly valuable for the realization of the spin battery. In such a device, it is of importance that the injecting electrode, and only the injecting electrode, is at resonance. The detecting electrode has to remain static to keep the measurements interpretable. By further tuning the resonance frequencies of the different electrode types, it is possible to reduce the field region of strong interaction. The wider the electrodes are, the lower the resonance frequency is. Making the short electrodes wider and the long electrodes narrower results in clearly separated resonances and in a simpler dynamic behavior in the interesting field region of small field magnitudes.

The well-known AMR is often used to probe static magnetization configurations.[32,33,35,36] With a comparably simple measurement setup and a tailored sample design, we used the AMR to study the dynamic process of the magnetization precession in the electrodes. The cone angle of individual electrodes was determined and we demonstrated that it depends on three parameters: the wider the electrodes, the narrower the CPW, and the smaller the external field, the larger is the cone angle. With a 3 μm-wide CPW and short electrodes, we obtained cone angles of up to 13.7°, which is considerably larger than the values reported in the literature so far.[24] In this reference, cone angles of up to 9° were achieved in a 300 nm-wide permalloy strip, which is the same value we determined in 250 nm-wide long electrodes. Within our sample design, the electrodes are placed on top of the CPW separated by an HSQ layer instead of placing them side-by-side as done, e.g., by Costache *et al.*[24] This provides the possibility to place the CPW and the electrodes closer together. The thickness of the HSQ layer can be further reduced by diluting the HSQ. Since in spin-pumping experiments the injected spin current increases with the cone angle,[25] large values are desirable.

*nkuhlman@physnet.uni-hamburg.de

[1] J. P. Park, P. Eames, D. M. Engebretson, J. Berezovsky, and P. A. Crowell, Phys. Rev. B **67**, 020403 (2003).

[2] H. Stoll, A. Puzic, B. van Waeyenberge, P. Fischer, J. Raabe, M. Buess, T. Haug, R. Höllinger, C. Back, D. Weiss, and G. Denbeaux, Appl. Phys. Lett. **84**, 3328 (2004).

[3] K. Perzlmaier, M. Buess, C. H. Back, V. E. Demidov, B. Hillebrands, and S. O. Demokritov, Phys. Rev. Lett. **94**, 057202 (2005).

[4] M. Grimsditch, G. K. Leaf, H. G. Kaper, D. A. Karpeev, and R. E. Camley, Phys. Rev. B **69**, 174428 (2004).

[5] R. Zivieri and F. Nizzoli, Phys. Rev. B **71**, 014411 (2005).

[6] B. A. Ivanov and C. E. Zaspel, Phys. Rev. Lett. **94**, 027205 (2005).

[7] J. Jorzick, S. O. Demokritov, C. Mathieu, B. Hillebrands, B. Bartenlian, C. Chappert, F. Rousseaux, and A. N. Slavin, Phys. Rev. B **60**, 15194 (1999).

[8] Y. Roussigné, S. M. Chérif, C. Dugautier, and P. Moch, Phys. Rev. B **63**, 134429 (2001).

[9] C. Bayer, J. Jorzick, B. Hillebrands, S. O. Demokritov, R. Kouba, R. Bozinoski, A. N. Slavin, K. Y. Guslienko, D. V. Berkov, N. L. Gorn, and M. P. Kostylev, Phys. Rev. B **72**, 064427 (2005).

[10] M. Bailleul, D. Olligs, and C. Fermon, Phys. Rev. Lett. **91**, 137204 (2003).

[11] C. Bayer, J. P. Park, H. Wang, M. Yan, C. E. Campbell, and P. A. Crowell, Phys. Rev. B **69**, 134401 (2004).

[12] M. Buess, R. Höllinger, T. Haug, K. Perzlmaier, U. Krey, D. Pescia, M. R. Scheinfein, D. Weiss, and C. H. Back, Phys. Rev. Lett. **93**, 077207 (2004).

[13] A. Vogel, A. Drews, T. Kamionka, M. Bolte, and G. Meier, Phys. Rev. Lett. **105**, 037201 (2010).

[14] H. Jung, K.-S. Lee, D.-E. Jeong, Y.-S. Choi, Y.-S. Yu, D.-S. Han, A. Vogel, L. Bocklage, G. Meier, M.-Y. Im, P. Fischer, and S.-K. Kim, Sci. Rep. **1**, 59 (2011).

[15] F. Giesen, J. Podbielski, T. Korn, M. Steiner, A. van Staa, and D. Grundler, Appl. Phys. Lett. **86**, 112510 (2005).

[16] A. Vogel, T. Kamionka, M. Martens, A. Drews, K. W. Chou, T. Tyliszczak, H. Stoll, B. van Waeyenberge, and G. Meier, Phys. Rev. Lett. **106**, 137201 (2011).

[17] F. J. Jedema, A. T. Filip, and B. J. van Wees, Nature (London) **410**, 345 (2001).

[18] A. van Staa, J. Wulfhorst, A. Vogel, U. Merkt, and G. Meier, Phys. Rev. B **77**, 214416 (2008).

[19] A. Vogel, J. Wulfhorst, and G. Meier, Appl. Phys. Lett. **94**, 122510 (2009).

[20] T. Kimura and M. Hara, Appl. Phys. Lett. **97**, 182501 (2010).

[21] Y. S. Gui, N. Mecking, X. Zhou, G. Williams, and C.-M. Hu, Phys. Rev. Lett. **98**, 107602 (2007).

[22] Y. Tserkovnyak, A. Brataas, and G. E. W. Bauer, Phys. Rev. Lett. **88**, 117601 (2002).

[23] A. Brataas, Y. Tserkovnyak, G. E. W. Bauer, and B. I. Halperin, Phys. Rev. B **66**, 060404 (2002).

[24] M. V. Costache, S. M. Watts, M. Sladkov, C. H. van der Wal, and B. J. van Wees, Appl. Phys. Lett. **89**, 232115 (2006).

[25] M. V. Costache, S. M. Watts, C. H. van der Wal, and B. J. van Wees, Phys. Rev. B **78**, 064423 (2008).

[26] T. L. Gilbert, IEEE Trans. Magn. **40**, 3443 (2004).

[27] T. J. Silva, C. S. Lee, T. M. Crawford, and C. T. Rogers, J. Appl. Phys. **85**, 7849 (1999).

[28] C. Kittel, Phys. Rev. **73**, 155 (1948).

[29] S. Mendach, J. Podbielski, J. Topp, W. Hansen, and D. Heitmann, Appl. Phys. Lett. **93**, 262501 (2008).

[30] S. Hankemeier, R. Frömter, N. Mikuszeit, D. Stickler, H. Stillrich, S. Pütter, E. Y. Vedmedenko, and H. P. Oepen, Phys. Rev. Lett. **103**, 147204 (2009).

[31] J. Topp, D. Heitmann, and D. Grundler, Phys. Rev. B **80**, 174421 (2009).

[32] L. Bocklage, B. Krüger, T. Matsuyama, M. Bolte, U. Merkt, D. Pfannkuche, and G. Meier, Phys. Rev. Lett. **103**, 197204 (2009).

[33] T. McGuire and R. Potter, IEEE Trans. Magn. **11**, 1018 (1975).

[34] A. Yamaguchi, K. Motoi, A. Hirohata, H. Miyajima, Y. Miyashita, and Y. Sanada, Phys. Rev. B **78**, 104401 (2008).

[35] M. Steiner, C. Pels, and G. Meier, J. Appl. Phys. **95**, 6759 (2004).

[36] T. G. S. M. Rijks, R. Coehoorn, M. J. M. de Jong, and W. J. M. de Jonge, Phys. Rev. B **51**, 283 (1995).